Petroleum Science 23 (2026) 1817–1828

Contents lists available at ScienceDirect

Petroleum Science

journal homepage: www.keaipublishing.com/en/journals/petroleum-science

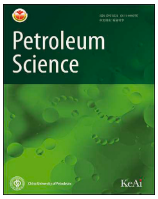

Original Paper

A new method for fluid saturation calculation in low resistivity oil reservoirs with nuclear magnetic resonance-constrained triple-water resistivity model

Xue-Juan Zhu [a,b], Shao-Gui Deng [a,b,*], Yi-Ren Fan [a,b], Xin-Min Ge [a,b], Zhou-Tuo Wei [a,b]

[a] *State Key Laboratory of Deep Oil and Gas, China University of Petroleum (East China), Qingdao, 266580, Shandong, China*
[b] *School of Geosciences, China University of Petroleum (East China), Qingdao, 266580, Shandong, China*

ARTICLE INFO

Article history:
Received 14 July 2025
Received in revised form
3 November 2025
Accepted 15 December 2025
Available online 19 December 2025

Edited by Meng-Jiao Zhou

Keywords:
Low resistivity oil reservoirs
Triple-water resistivity model
Nuclear magnetic resonance (NMR) logging
Fluid saturation calculation

ABSTRACT

To address the evaluation difficulty of hydrocarbon saturation in low resistivity reservoirs, an innovative method for calculating oil saturation is proposed using a nuclear magnetic resonance (NMR)-constrained triple-water resistivity model. This model explicitly distinguishes three conductive water phases: movable water, capillary-bound water, and clay-bound water. Resistivity response equations are established for both water-saturated and hydrocarbon-bearing rocks. A cooperative inversion framework is proposed based on NMR and conventional logging data, incorporating high-precision NMR-derived parameters as constraints during conventional logging inversion. The pore component volumes are obtained with the NMR T_2 spectrum decomposition and served as a priori information for the nonlinear optimization of porosity exponents. This enables the construction of a pore component inversion algorithm using conventional logging data, thereby extending water saturation calculation applicability in complex reservoirs. The method incorporates data-driven optimization to effectively reduce the reliance on core-based calibration data (mercury injection, petrophysical experiments, cation exchange capacity (CEC) tests). Application in a Bohai Bay Basin low resistivity reservoir demonstrates superior saturation calculation accuracy compared to traditional models. The integration of multi-physics logging inversion with nonlinear optimization effectively enhances conductivity mechanism characterization in reservoirs with complex pore systems, providing a robust technical solution for quantitative evaluation of low resistivity oil reservoirs.

1. Introduction

The Archie's equation-based log interpretation system (Archie, 1942) has served as the cornerstone for quantitative hydrocarbon saturation evaluation since its inception. However, as exploration targets increasingly shift toward complex reservoirs, significant non-Archie phenomena emerge in low porosity and low resistivity reservoirs (Zhang et al., 2012; Simanjuntak et al., 2020). In response, scholars have developed successive petrophysical models including the Waxman-Smits (W-S) model (Waxman and Smits, 1968), laminated sand-shale resistivity model (Poupon and Leveaux, 1971), and Dual-Water Model (Clavier et al., 1984). In recent years, deeper insights into reservoir complexity have driven the development of multi-component conductivity theories and dual/triple porosity models. These models provide a more accurate characterization of resistivity in reservoirs with complex pore systems and conductive media (Aguilera and Aguilera, 2003, 2009; Aguilera, 2004; Al-Ghamdi et al., 2011; Dash and Heidari, 2022). Among them, triple porosity models are particularly valuable as they account for the distinct conductive contributions from three pore systems—such as matrix pores, fractures, and isolated vugs—whose properties (e.g., size, shape, and distribution) vary significantly (Iheanacho, 2013; Bukola, 2013; Wei et al., 2023; Hu et al., 2024; Jia et al., 2024). While these advancements enhanced saturation quantification accuracy in conventional shaly sandstone reservoirs, three critical limitations persist when addressing microporosity-dominated low resistivity reservoirs: (1)

---

[*] Corresponding author
E-mail address: dengshg@upc.edu.cn (S.-G. Deng).
Peer review under the responsibility of China University of Petroleum (Beijing).

https://doi.org/10.1016/j.petsci.2025.12.026

insufficient differentiation between macroporosity and microporosity conductivity mechanisms, (2) oversimplified assumptions regarding the transient state of clay-bound water, and (3) inadequate consideration of pore structure fractal characteristics influencing resistivity responses.

To better characterize the resistivity contributions of distinct water phases, we enhanced the conventional "triple porosity" model for argillaceous sandstones into the triple-water resistivity model (hereafter termed the triple-water model). Initially proposed by Li et al. (2000) and Mo et al. (2001, 2005), this model categorizes conductive reservoir fluids into three components: (1) free flowing water in macropores (hereafter termed movable water), (2) capillary-bound water in micropores, and (3) clay-bound water adsorbed in clay interlayers through hydration (clay-bound water). The model establishes distinct conductive mechanisms: ionic conduction governs movable and capillary-bound water, while cation exchange dominates clay-bound water conductivity, with total rock conductivity representing the parallel contribution of these three phases (Li et al., 2000). By explicitly differentiating the conductive properties of movable water, capillary-bound water, and clay-bound water, the triple-water model improves the characterization of heterogeneous conductive media (Mo et al., 2001; Huang, 2005; Ding, 2005; Xu, 2012; Zhang et al., 2023). However, practical implementation faces challenges due to ambiguous definitions of the three water-phase states and the requirement for extensive core-derived calibration data (e.g., mercury injection, cation exchange capacity, and petrophysical experiments) to constrain multiple modeling parameters (Mo et al., 2005; Guo et al., 2015; Zhang et al., 2010, 2011, 2023; Tariq et al., 2018; Kang et al., 2023), significantly hindering its field application and broader adoption.

Nuclear magnetic resonance (NMR) logging detects the nuclear magnetic resonance phenomena of hydrogen atoms and employs multiple acquisition modes to highlight differences in the relaxation properties of various fluids. This enables the characterization of reservoir pore structures, fluid types, and content. A key advantage of NMR logging is its independence from rock matrix composition, allowing direct identification of oil and gas under in-situ conditions, as well as quantitative differentiation between movable and irreducible fluids. Despite its capability to provide high-resolution insights into pore systems and fluid properties, NMR logging is associated with relatively high costs, making it less feasible for widespread application in all wells. In contrast, conventional logging data are more readily available but offer limited accuracy, which restricts their utility for detailed evaluation of complex reservoirs.

Building upon this foundation, this paper establishes an integrated NMR-conventional logging inversion framework that synergistically combines the high-resolution data from NMR logging with the broad applicability of conventional logs. This approach employs machine learning algorithms and optimization techniques to jointly invert triple-water model parameters, thereby enhancing saturation computation accuracy. Specifically, NMR T_2 spectra are utilized to quantify movable fluid, microporosity, and clay-bound water volumes, which are integrated as a priori constraints into the triple-water model. Subsequently, adaptive optimization algorithms dynamically resolve porosity exponents and saturation exponent, effectively reducing reliance on discrete experimental datasets inherent to traditional methods. By leveraging intrinsic correlations within logging data through automated conductive component optimization, the methodology minimizes external parameter dependencies. The framework uniquely incorporates NMR logging constraints as physical drivers grounded in the triple-water model theory, enabling robust computation even with limited training samples (Zhang et al., 2022). This innovative integration provides a transformative workflow for water saturation determination in argillaceous sandstone reservoirs, particularly addressing low resistivity reservoirs affected by clay-induced excess conductivity.

2. Parameter calculation method of triple-water model

2.1. Construction of the triple-water model

The triple-water model is grounded in parallel conductivity theory, which asserts that rock conductivity arises from three distinct water phases (Fig. 1): (1) clay-bound water, (2) capillary-bound water, and (3) movable water. Clay-bound water is immobilized by adsorption onto clay particle surfaces, conducting solely via cation exchange, and its volume equals the clay-associated pore space. Capillary-bound water occupies microscopic pores within the formation matrix, remaining immobile under typical reservoir conditions, with its volume corresponding to microporosity. Movable water resides in macropores and demonstrates pressure-driven mobility. For hydrocarbon-bearing rocks, the model postulates that hydrocarbons selectively displace movable water within macropores while preserving both capillary-bound water and clay-bound water. Consequently, total water saturation S_w is defined as:

$$S_{\mathrm{w}} = \frac{V_{\mathrm{wf}} + V_{\mathrm{wi}} + V_{\mathrm{wc}}}{\phi_{\mathrm{f}} + \phi_{\mathrm{i}} + \phi_{\mathrm{c}}} = \frac{\phi_{\mathrm{f}} \cdot S_{\mathrm{wf}} + \phi_{\mathrm{i}} + \phi_{\mathrm{c}}}{\phi} \tag{1}$$

where S_{wf} represents the water saturation in macropores, which corresponds to the percentage of movable water volume occupying the macropores; V_{wc}, V_{wi} and V_{wf} are the volume fractions of clay-bound water, capillary-bound water, and movable water, respectively; ϕ_{c}, ϕ_{i} and ϕ_{f} denote the clay-associated porosity, micro-capillary porosity, and macroporosity, respectively. In a unit volume of rock, $V_{\mathrm{wc}} = \phi_{\mathrm{c}}$, $V_{\mathrm{wi}} = \phi_{\mathrm{i}}$, $V_{\mathrm{wf}} = \phi_{\mathrm{f}} \cdot S_{\mathrm{wf}}$; ϕ denotes the total porosity of the rock.

The triple-water model derives its theoretical foundation from multi-phase parallel conductivity principles. For fully water-saturated rocks, the total conductivity C_0 is formulated as:

$$C_0 = \frac{1}{R_0} = \frac{\phi_{\mathrm{f}}^{m_{\mathrm{f}}}}{R_{\mathrm{wf}}} + \frac{\phi_{\mathrm{i}}^{m_{\mathrm{i}}}}{R_{\mathrm{wi}}} + \frac{\phi_{\mathrm{c}}^{m_{\mathrm{c}}}}{R_{\mathrm{wc}}} \tag{2}$$

In hydrocarbon-bearing formations, where hydrocarbons exclusively occupy macropores, the conductivity C_{t} becomes:

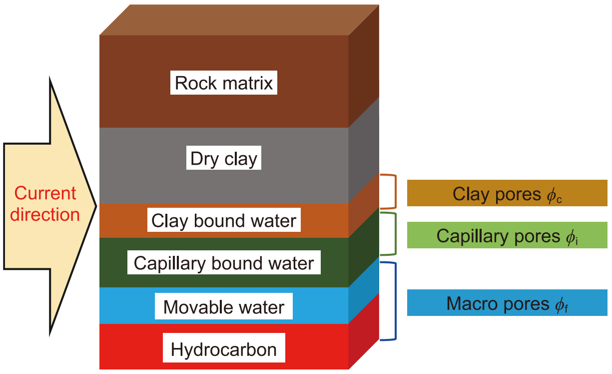

Fig. 1. Triple-water model theoretical diagram.

$$C_{\mathrm{t}} = \frac{1}{R_{\mathrm{t}}} = \frac{\phi_{\mathrm{f}}^{m_{\mathrm{f}}} \cdot S_{\mathrm{wf}}^{n_{\mathrm{f}}}}{R_{\mathrm{wf}}} + \frac{\phi_{\mathrm{i}}^{m_{\mathrm{i}}}}{R_{\mathrm{wi}}} + \frac{\phi_{\mathrm{c}}^{m_{\mathrm{c}}}}{R_{\mathrm{wc}}} \tag{3}$$

where C_0 and R_0 are the conductivity (in S/m) and resistivity (in $\Omega\cdot$m) of water-saturated rocks; C_{t} and R_{t} are the conductivity (in S/m) and resistivity (in $\Omega\cdot$m) of hydrocarbon-bearing rocks; the meanings of ϕ_{c}, ϕ_{i}, ϕ_{f} and S_{wf} are the same as in Eq. (1); m_{f}, m_{i}, and m_{c} are porosity exponents for respective pore systems, representing the tortuosity of the pore networks. Their physical meaning is the same as that of the Archie exponent "m"; however, while "m" in Archie's equation reflects the overall pore structure of the rock, m_{f}, m_{i}, and m_{c} respectively represent the tortuosities associated with different types of pores within the rock; n_{f} is the saturation exponent quantifying hydrocarbon distribution effects. Its physical meaning aligns with that of the exponent "n" in Archie's equation, representing the micro heterogeneity of saturation distribution and characterizing the distribution of oil and water within the pores as well as the surface conductive properties of the rock, with the distinction that n_{f} specifically describes the oil-water distribution in macropores; R_{wf}, R_{wi}, and R_{wc} denote the resistivity of movable water, capillary-bound water, and clay-bound water, respectively.

2.2. Determination of porosity exponents (m_{f}, m_{i}, m_{c})

NMR logging directly characterizes formation pore architecture and fluid mobility by analyzing hydrogen nucleus relaxation behavior, enabling precise quantification of clay-bound water, capillary-bound water, and movable water volumes (Fig. 2). In water-saturated zones, multiple logging points were selected to extract clay-bound water, capillary-bound water, and movable water volumes alongside corresponding deep resistivity (R_0) measurements. These datasets were incorporated into the water-saturated conductivity equation (Eq. (2)), generating an over-determined system of equations (Eq. (5)). The conductivity of movable water and capillary-bound water is governed by ionic conduction ($R_{\mathrm{wf}} = R_{\mathrm{wi}}$), determined through formation water salinity analysis or calculated via Archie's equation and spontaneous potential (SP) interpretation. In contrast, clay-bound water conductivity (R_{wc}) depends on cation exchange capacity (CEC), calculated using temperature-dependent relationships (Eqs. (6)–(9)). Substituting R_{wc}, R_{wi}, R_{wf} and their corresponding porosities (ϕ_{c}, ϕ_{i}, ϕ_{f}) into Eq. (5) yields a nonlinear system with porosity exponents (m_{c}, m_{i}, m_{f}) as unknowns. This system is solved through constrained least-squares optimization:

$$\min \sum_{k=1}^{N} \left[C_{0,k} - \left(\frac{\phi_{\mathrm{f},k}^{m_{\mathrm{f}}}}{R_{\mathrm{wf},k}} + \frac{\phi_{\mathrm{i},k}^{m_{\mathrm{i}}}}{R_{\mathrm{wi},k}} + \frac{\phi_{\mathrm{c},k}^{m_{\mathrm{c}}}}{R_{\mathrm{wc},k}} \right) \right]^2 \tag{4}$$

where N represents the number of calibration points. Regularization techniques ensure solution stability when addressing collinearity between pore systems. In this analysis, the porosity exponents were determined using the ordinary least squares (OLS) method. To ensure robustness under large-sample conditions, outliers were removed using the standard score (z-score) method based on the 3σ criterion.

$$\begin{cases} \dfrac{1}{R_{01}} = \dfrac{\phi_{\mathrm{f1}}^{m_{\mathrm{f}}}}{R_{\mathrm{wf}}} + \dfrac{\phi_{\mathrm{i1}}^{m_{\mathrm{i}}}}{R_{\mathrm{wi}}} + \dfrac{\phi_{\mathrm{c1}}^{m_{\mathrm{c}}}}{R_{\mathrm{wc}}} \\ \dfrac{1}{R_{02}} = \dfrac{\phi_{\mathrm{f2}}^{m_{\mathrm{f}}}}{R_{\mathrm{wf}}} + \dfrac{\phi_{\mathrm{i2}}^{m_{\mathrm{i}}}}{R_{\mathrm{wi}}} + \dfrac{\phi_{\mathrm{c2}}^{m_{\mathrm{c}}}}{R_{\mathrm{wc}}} \\ \dfrac{1}{R_{03}} = \dfrac{\phi_{\mathrm{f3}}^{m_{\mathrm{f}}}}{R_{\mathrm{wf}}} + \dfrac{\phi_{\mathrm{i3}}^{m_{\mathrm{i}}}}{R_{\mathrm{wi}}} + \dfrac{\phi_{\mathrm{c3}}^{m_{\mathrm{c}}}}{R_{\mathrm{wc}}} \\ \vdots \\ \dfrac{1}{R_{0N}} = \dfrac{\phi_{\mathrm{f}N}^{m_{\mathrm{f}}}}{R_{\mathrm{wf}}} + \dfrac{\phi_{\mathrm{i}N}^{m_{\mathrm{i}}}}{R_{\mathrm{wi}}} + \dfrac{\phi_{\mathrm{c}N}^{m_{\mathrm{c}}}}{R_{\mathrm{wc}}} \end{cases} \tag{5}$$

$$R_{\mathrm{wc}} = \alpha \cdot V_{\mathrm{q}} / \beta \tag{6}$$

$$\beta = 0.0857 \cdot T - 0.143 \tag{7}$$

$$\alpha = \begin{cases} 1, P_{\mathrm{w}} > P_{\mathrm{w0}} \\ \sqrt{\dfrac{P_{\mathrm{w0}}}{P_{\mathrm{w}}}}, \quad P_{\mathrm{w}} < P_{\mathrm{w0}} \end{cases} \tag{8}$$

$$V_{\mathrm{q}} = \frac{1}{2.853 + 0.019 \cdot T} \tag{9}$$

In Eqs. (6)–(9), R_{wc} denotes the resistivity of clay-bound water. The symbol α denotes the diffusion factor of the Na^+ diffusion layer, while β represents the equivalent conductivity of compensating Na^+ ions in clay-bound water. V_{q} signifies the pore volume

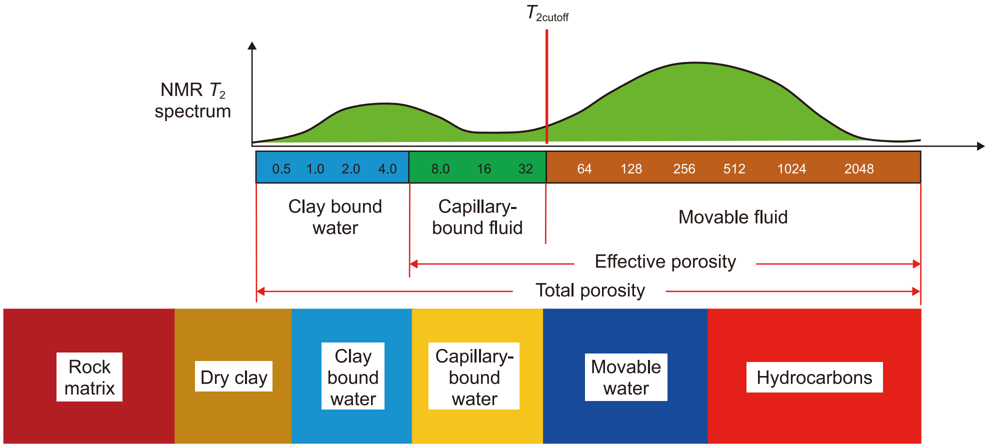

Fig. 2. Nuclear magnetic resonance logging characterizes pore volume.

occupied by clay-bound water at a given cation exchange capacity (CEC) of the clay, and this volume depends exclusively on the formation temperature. P_{w0} represents the salinity of the formation water when the thickness of the diffusion layer on the clay surface is at its minimum, approximately 0.35 mol/cm^3, which is equivalent to a NaCl salinity of 20,475 mg/L. P_{w} denotes the actual salinity of the formation water, and T represents the formation temperature in degrees Celsius (in °C).

2.3. NMR-constrained conventional logging integration

While NMR logging provides direct quantification of fluid volumes with high precision, its application is typically restricted to key wells within a reservoir study area given its operational costs. To enable triple-water model implementation across all wells, conventional logging data are integrated with NMR-derived porosity exponents (m_{f}, m_{i}, m_{c}) through a constrained inversion framework. The NMR-calibrated exponents serve as a priori constraints during conventional log interpretation, ensuring physical fidelity of model parameters while maintaining geological consistency across both cored and uncored intervals. This hybrid approach preserves the petrophysical rigor of the triple-water model while achieving cost-effective field-scale deployment.

2.3.1. Triple-water model based on conventional logging

In shaly sandstone formations, the normalized volume of clay-bound water is expressed as:

$$V_{\phi\mathrm{cw}} = \alpha \cdot V_{\mathrm{q}} \cdot Q_{\mathrm{v}} \tag{10}$$

where $V_{\phi\mathrm{cw}}$ is the volume of clay-bound water per unit pore volume; the meanings of α and V_{q} are the same as in Eq. (6). Q_{v} denotes cation exchange capacity (in meq/cm^3), measured as sodium ion equivalents per total pore volume, given that Q_{v} is directly proportional to shale content (V_{sh}), the clay-bound water porosity (ϕ_{c}) for formations with total porosity ϕ becomes:

$$\phi_{\mathrm{c}} = \phi \cdot V_{\phi\mathrm{cw}} = \phi \cdot \alpha \cdot V_{\mathrm{q}} \cdot A \cdot V_{\mathrm{sh}} \tag{11}$$

The empirical coefficient A, designated as the clay-bound water volumetric coefficient, quantifies clay-bound water storage capacity in argillaceous formations. Within defined stratigraphic intervals of a given basin, where clay mineral assemblages exhibit consistent composition and spatial distribution, A is treated as a geologically invariant parameter.

$$\begin{cases} \dfrac{1}{R_{01}} = \dfrac{1}{R_{\mathrm{w}}}(\phi_1 - \phi_1 \cdot S_{\mathrm{wi1}})^{m_{\mathrm{f}}} + \dfrac{1}{R_{\mathrm{w}}}(\phi_1 \cdot S_{\mathrm{wi1}} - \phi_1 \cdot \alpha \cdot V_{\mathrm{q}} \cdot A \cdot V_{\mathrm{sh1}})^{m_{\mathrm{i}}} + \dfrac{1}{R_{\mathrm{wc1}}}(\phi_1 \cdot \alpha \cdot V_{\mathrm{q}} \cdot A \cdot V_{\mathrm{sh1}})^{m_{\mathrm{c}}} \\ \dfrac{1}{R_{02}} = \dfrac{1}{R_{\mathrm{w}}}(\phi_2 - \phi_2 \cdot S_{\mathrm{wi2}})^{m_{\mathrm{f}}} + \dfrac{1}{R_{\mathrm{w}}}(\phi_2 \cdot S_{\mathrm{wi2}} - \phi_2 \cdot \alpha \cdot V_{\mathrm{q}} \cdot A \cdot V_{\mathrm{sh2}})^{m_{\mathrm{i}}} + \dfrac{1}{R_{\mathrm{wc2}}}(\phi_2 \cdot \alpha \cdot V_{\mathrm{q}} \cdot A \cdot V_{\mathrm{sh2}})^{m_{\mathrm{c}}} \\ \dfrac{1}{R_{03}} = \dfrac{1}{R_{\mathrm{w}}}(\phi_3 - \phi_3 \cdot S_{\mathrm{wi3}})^{m_{\mathrm{f}}} + \dfrac{1}{R_{\mathrm{w}}}(\phi_3 \cdot S_{\mathrm{wi3}} - \phi_3 \cdot \alpha \cdot V_{\mathrm{q}} \cdot A \cdot V_{\mathrm{sh3}})^{m_{\mathrm{i}}} + \dfrac{1}{R_{\mathrm{wc3}}}(\phi_3 \cdot \alpha \cdot V_{\mathrm{q}} \cdot A \cdot V_{\mathrm{sh3}})^{m_{\mathrm{c}}} \\ \vdots \\ \dfrac{1}{R_{0N}} = \dfrac{1}{R_{\mathrm{w}}}(\phi_N - \phi_N \cdot S_{\mathrm{wi}N})^{m_{\mathrm{f}}} + \dfrac{1}{R_{\mathrm{w}}}(\phi_N \cdot S_{\mathrm{wi}N} - \phi_N \cdot \alpha \cdot V_{\mathrm{q}} \cdot A \cdot V_{\mathrm{sh}N})^{m_{\mathrm{i}}} + \dfrac{1}{R_{\mathrm{wc}N}}(\phi_N \cdot \alpha \cdot V_{\mathrm{q}} \cdot A \cdot V_{\mathrm{sh}N})^{m_{\mathrm{c}}} \end{cases} \tag{15}$$

Conventional log-derived irreducible water saturation (S_{wi}) inherently incorporates both clay-bound water and capillary-bound water. The capillary-bound water volume (ϕ_{i}) is therefore calculated by subtracting clay-bound water porosity (ϕ_{c}) from total irreducible water porosity:

$$\phi_{\mathrm{i}} = \phi \cdot S_{\mathrm{wi}} - \phi_{\mathrm{c}} \tag{12}$$

Macroporosity (ϕ_{f}) is derived by subtracting total bound water volume from bulk porosity:

$$\phi_{\mathrm{f}} = \phi - \phi_{\mathrm{i}} - \phi_{\mathrm{c}} = \phi(1 - S_{\mathrm{wi}}) \tag{13}$$

Here ϕ is computed from conventional logs (neutron-density crossplot or acoustic-physical models), while S_{wi} is determined through empirical relationships incorporating shale volume (V_{sh}), porosity-permeability trends, and capillary pressure analogs.

The triple-water model for water-saturated formations is thus fully parameterized using conventional logging inputs:

$$\frac{1}{R_0} = \frac{1}{R_{\mathrm{w}}}(\phi - \phi \cdot S_{\mathrm{wi}})^{m_{\mathrm{f}}} + \frac{1}{R_{\mathrm{w}}}(\phi \cdot S_{\mathrm{wi}} - \phi \cdot \alpha \cdot V_{\mathrm{q}} \cdot A \cdot V_{\mathrm{sh}})^{m_{\mathrm{i}}} + \frac{1}{R_{\mathrm{wc}}}(\phi \cdot \alpha \cdot V_{\mathrm{q}} \cdot A \cdot V_{\mathrm{sh}})^{m_{\mathrm{c}}} \tag{14}$$

2.3.2. NMR-constrained determination of clay-bound water volumetric coefficient (*A*)

Within the water-saturated intervals identified in Section 2.2, conventional logging data are analyzed to calculate parameters including total porosity (ϕ), irreducible water saturation (S_{wi}), shale content (V_{sh}), and empirical coefficients (α, V_{q}). Combined with the predetermined porosity exponents (m_{f}, m_{i}, m_{c}), these parameters are incorporated into Eq. (14) to establish an NMR-constrained overdetermined system (Eq. (15)). The clay-bound water volumetric coefficient A is subsequently resolved as the least-squares solution to this system, computed via least-squares optimization. The coefficient α exhibits dependence on formation water salinity. Formation water resistivity (R_{w}) is predominantly salinity-controlled but temperature-sensitive, while clay-bound water resistivity (R_{wc}) and V_q are temperature-dependent. Consequently, for datasets with minimal depth variations across measurement points (N), α, V_{q}, and R_{w} may be treated as constants. In contrast, formations exhibiting substantial depth-dependent heterogeneity or geologically driven variations in fluid properties require depth-specific parameterization.

2.4. Determination of saturation exponent n_f

Building upon Eq. (3) and the methodology established in Section 2.3, the triple-water resistivity model for hydrocarbon-

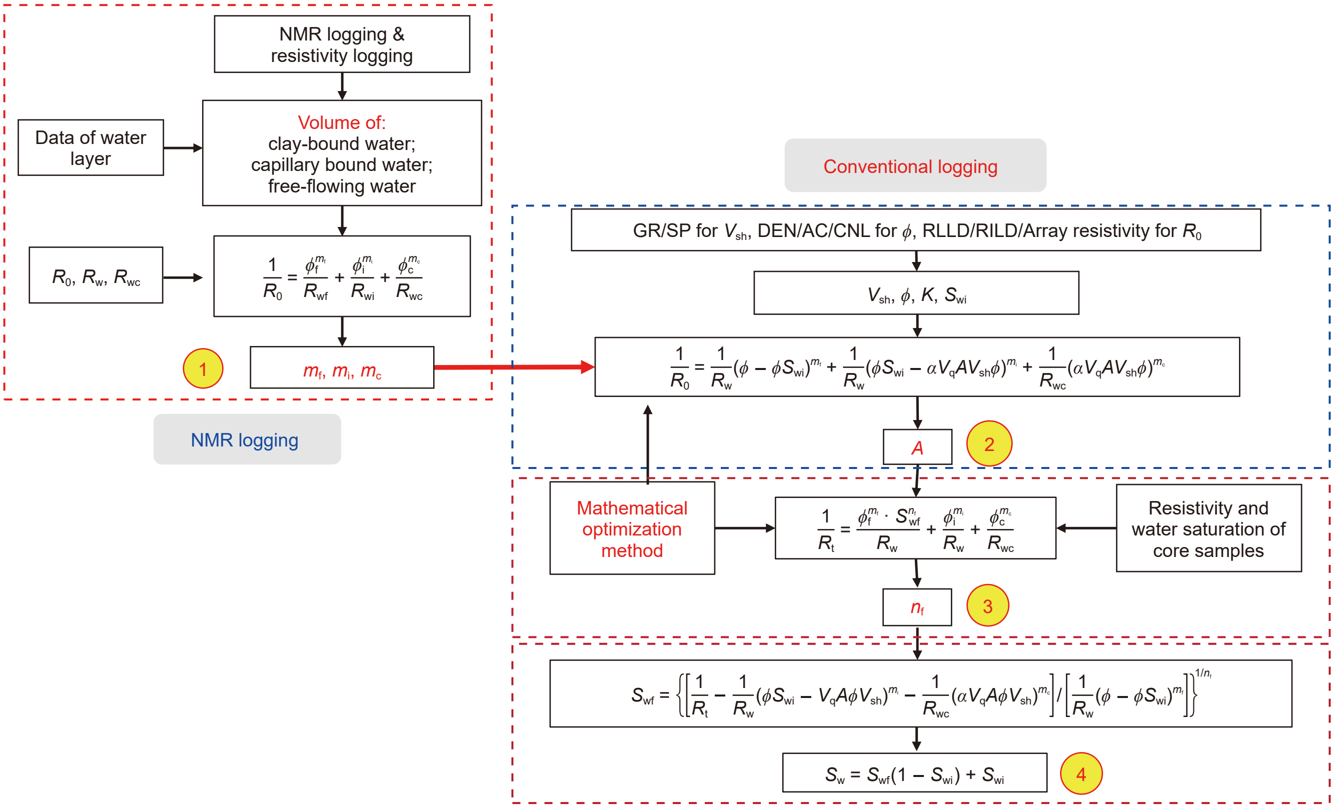

Fig. 3. Parameterization workflow for triple-water resistivity model.

bearing formations is parameterized using conventional logging data:

$$\frac{1}{R_t}=\frac{1}{R_w}(\phi-\phi\cdot S_{wi})^{m_f}\cdot S_{wf}^{n_f}+\frac{1}{R_w}(\phi\cdot S_{wi}-\phi\cdot\alpha\cdot V_q\cdot A\cdot V_{sh})^{m_i}+\frac{1}{R_{wc}}(\phi\cdot\alpha\cdot V_q\cdot A\cdot V_{sh})^{m_c} \tag{16}$$

Multiple sealed core samples from hydrocarbon zones are analyzed to determine total water saturation (S_w), which is converted to movable water saturation (S_{wf}). Deep resistivity (R_t) measurements are matched to core depths, while conventional log-derived parameters (ϕ, S_{wi}, V_{sh}, α, V_q) are computed. These parameters, combined with previously resolved coefficients (m_f, m_i, m_c, A), are incorporated into Eq. (16), generating an overdetermined system in which n_f is the only unknown. The saturation exponent is subsequently determined through least-squares minimization.

This study establishes a systematic workflow for determining triple-water model parameters and hydrocarbon saturation (Fig. 3), comprising four sequential stages:

Step 1: Porosity exponent derivation: Derive porosity exponents m_f, m_i and m_c through NMR log analysis of water-saturated intervals.
Step 2: Clay-bound water volumetric coefficient calibration: Construct the water-saturated formation triple-water model using conventional logs, and determine the clay-bound water volumetric coefficient (A) with NMR-derived m_f, m_i, and m_c as constraints.
Step 3: Saturation exponent determination: Implement the hydrocarbon-bearing formation triple-water model by integrating oil-saturated core resistivity measurements and oil saturation data, to solve for movable water saturation exponent n_f.
Step 4: Field-scale saturation computation: Calculate water saturation across all wells using fully parameterized triple-water model inputs (m_f, m_i, m_c, A, n_f) combined with conventional log-derived reservoir properties (porosity ϕ, shale volume V_{sh}, irreducible water saturation S_{wi}).

3. Field application and efficacy validation

To validate the practical applicability of the proposed methodology, this paper applies the triple-water model in a low-resistivity reservoir within the southern Huanghua Depression of Bohai Bay Basin. The target reservoir, situated in the Paleocene Kongdian Formation, is characterized by a rift lacustrine basin depositional system dominated by braided river delta front subfacies. Reservoir architecture comprises underwater distributary channels and mouth bar microfacies, exhibiting low-porosity and low-permeability characteristics with moderate heterogeneity (coefficient of variation = 0.71).

3.1. Reservoir geological characteristics

3.1.1. Lithology, petrophysical properties, and pore structure

The reservoir lithology comprises siltstones and fine-grained sandstones with elevated feldspar content coupled with low compositional and textural maturity. Rock types are classified as arkosic sandstones and lithic arkoses (Fig. 4(a)). High matrix content (average 11.56%, Fig. 4(b)) dominated by argillaceous matrix is observed. Scanning electron microscopy reveals significant mineral alteration-induced clay authigenesis, abundant

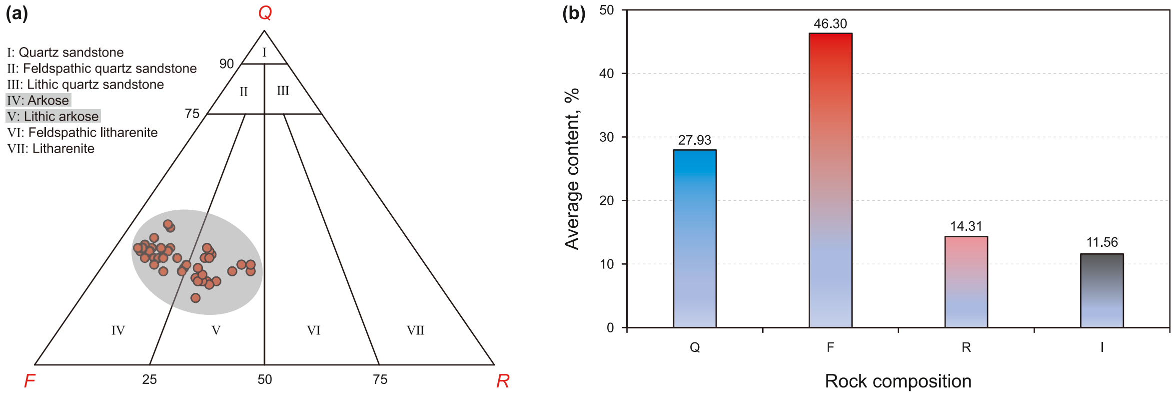

Fig. 4. Rock types and average content of rock components. **(a)** Ternary diagram of rock composition. **(b)** Histogram of rock component content. Notes: Q: quartz; F: feldspar; R: rock fragments; I: Interstitial materials. 50 core samples are included.

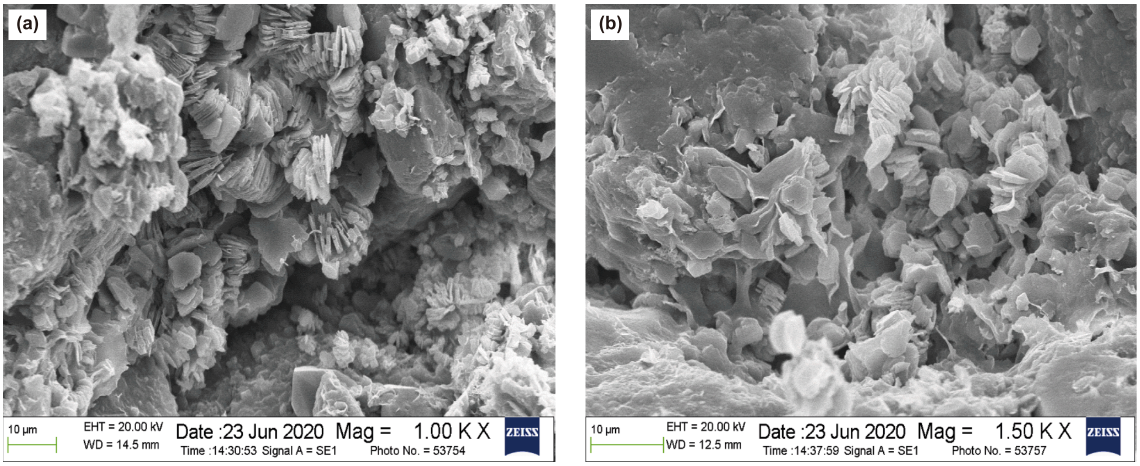

Fig. 5. Scanning electron microscope characteristics. **(a)** Scalar kaolinite, authigenic quartz and illite filling intergranular pores. **(b)** Filamentous illite, scaly kaolinite and authigenic quartz fill intergranular pores.

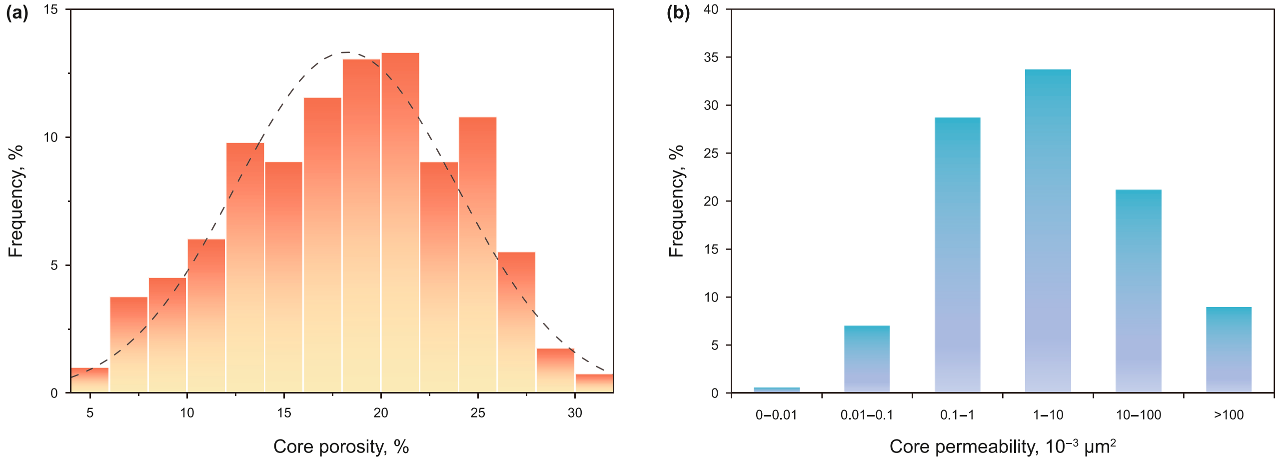

Fig. 6. The characteristics of reservoir porosity and permeability (360 core samples). **(a)** The porosity distribution histogram, **(b)** the permeability distribution histogram.

argillaceous debris, and well-developed platy kaolinite-illite intergrowths (Fig. 5).

Core porosity predominantly ranges from 14% to 26%, with permeability spanning 0.1 to 100 × 10^{-3} μm^2, classifying the reservoir as medium-porosity and medium-low-permeability (Fig. 6). NMR experimental results demonstrate a single-peak pore structure dominated by micropores. Minor divergence between centrifuged and fully water-saturated core T_2 spectra indicates limited movable fluid content and elevated bound water saturation (Fig. 7). Mercury injection capillary pressure curves exhibit

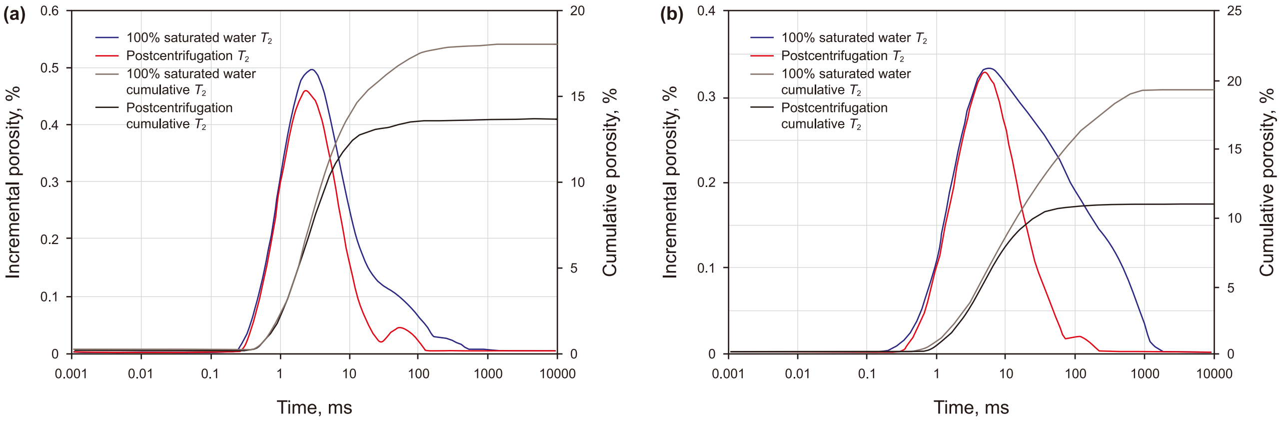

Fig. 7. Core nuclear magnetic resonance T_2 spectrum characteristics. (**a**) Core 1: Residual water saturation 74.2%. (**b**) Core 2: Residual water saturation 44%.

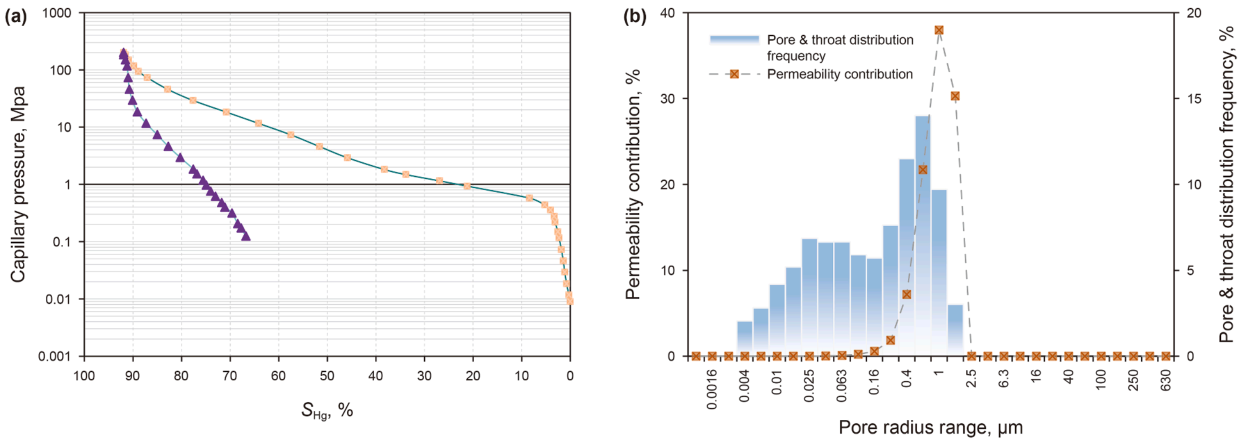

Fig. 8. Core mercury intrusion porosimetry data. (**a**) Mercury intrusion capillary curve. (**b**) Pore radius distribution and permeability contribution.

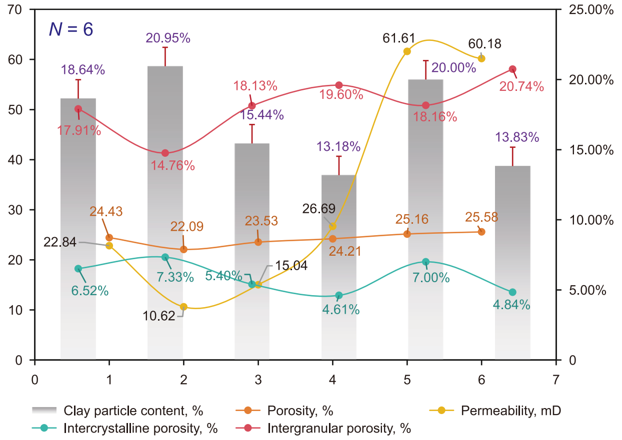

Fig. 9. Clay mineral content and clay pore ratio.

fine skewness with a concentrated small-aperture pore-throat distribution contributing negligibly to permeability, indicative of restricted fluid mobility (Fig. 8). Integrated analysis of thin sections, scanning electron microscopy, and petrophysical data reveals high clay particle volume fractions, abundant clay intergranular pores, and strong permeability dependence on intergranular pore connectivity (Fig. 9).

3.1.2. *Resistivity characteristics of hydrocarbon zones*

Comparative analysis of oil-water layer responses in the study area reveals resistivity distributions of 3–10 Ω m for oil zones, 2–5 Ω m for water zones, and 3–6 Ω m for oil-water transition zones. The low resistivity contrast between oil and water zones (Fig. 10) is characteristic of low-resistivity-contrast reservoirs. For instance, Layers 11–13 (oil zone), Layer 20 (water zone), and Layer 22 (oil-water zone) exhibit comparable total porosity and resistivity values. NMR-based fluid typing indicates that oil zone pore spaces are dominated by immobile capillary-bound water, clay-bound water, and hydrocarbons, with negligible movable water saturation. This configuration results in oil production despite elevated water saturation—a key factor in the genesis of low-resistivity reservoirs. Layer 37 (water zone) demonstrates similar porosity to Layer 20 but significantly lower resistivity. NMR analysis differentiates their conductive mechanisms: Layer 20 contains predominantly capillary-bound water, while Layer 37 hosts substantial movable water. This contrast highlights the divergent conductivity contributions of movable water relative to bound water phases.

Fig. 11 shows the porosity, bound water saturation, and corresponding resistivity measurements from oil-bearing core analyses. Crossplot analysis demonstrates a positive correlation between resistivity and porosity, in contrast to an inverse relationship with bound water saturation. This indicates that while higher porosity correlates with elevated hydrocarbon saturation, a concurrent increase in bound water saturation significantly suppresses

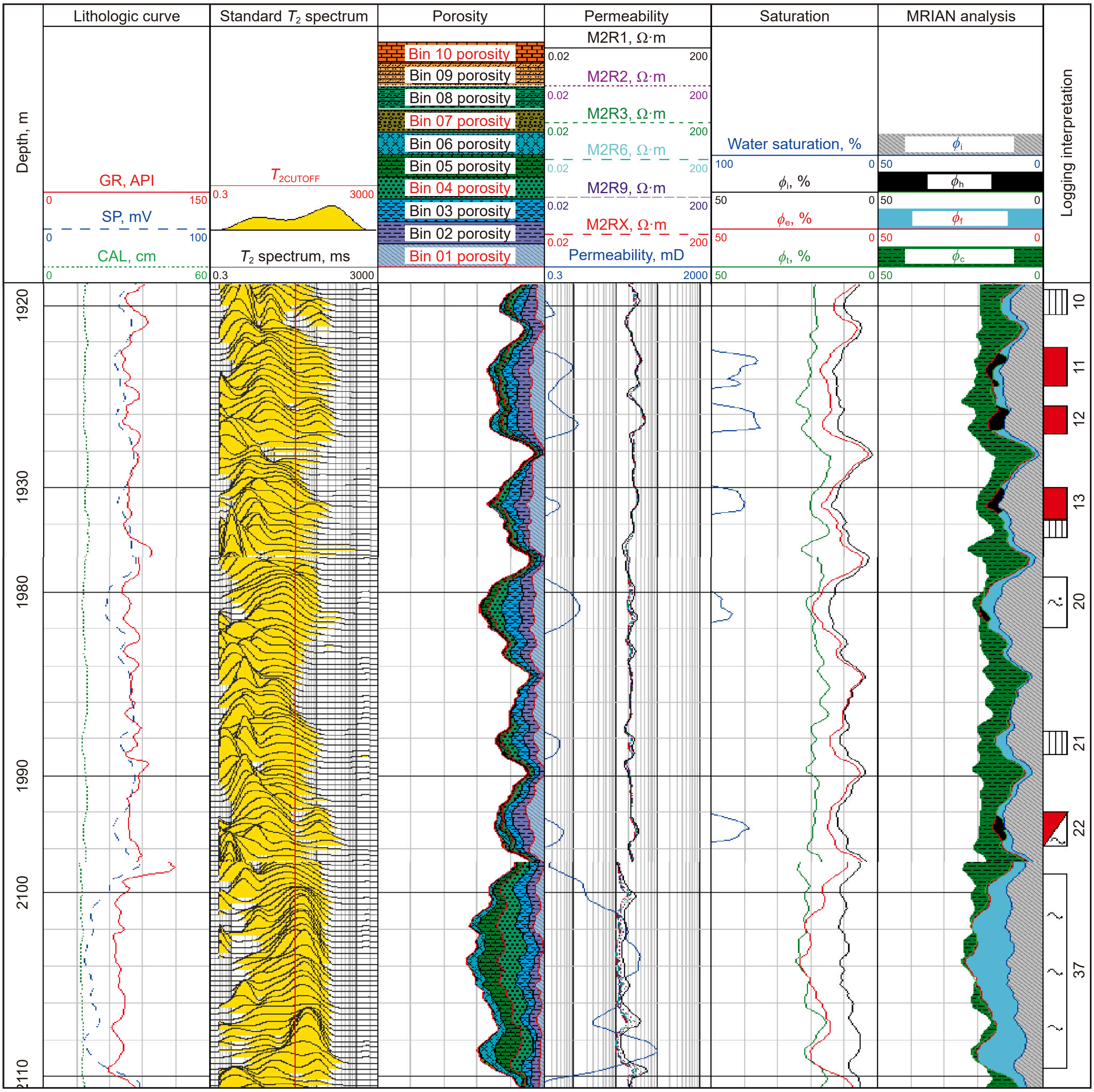

Fig. 10. Reservoir logging response characteristics.

resistivity. Integrated analysis reveals that reservoirs in the study area are characterized by high bound water content and low resistivity, with distinct conductivity contributions from different water phases. Consequently, accurate water saturation calculation requires: (1) independent characterization of conductive mechanisms for each water type; (2) quantitative assessment of pore water volume distributions; (3) explicit modeling of the influence of pore water on bulk conductivity. Notably, despite available lithological and petrophysical experimental data, several critical limitations persist: inadequate mercury injection capillary pressure (MICP) and NMR datasets; and the lack of petrophysical-electrical (Archie's parameter) and cation exchange capacity (CEC) measurements. These constraints prevent direct determination of pore component fractions and associated petrophysical parameters, thus necessitating the triple-water model parameterization methodology outlined in this study (Fig. 3) prior to saturation computation.

3.2. Parameter calculation and result analysis

3.2.1. Triple-water model parameterization

Following the methodology in Section 2, 11 water-saturated intervals (2400–2500 m depth) from Well A were analyzed using NMR interpretation results and core data. For 2690 logging depth points, clay-bound water, capillary-bound water, and movable water volumes (ϕ_c, ϕ_i, ϕ_f) were quantified alongside depth-correlated resistivity (R_0). Formation water analysis indicates $NaHCO_3$-type water with total salinity averaging 31248.5 mg/L

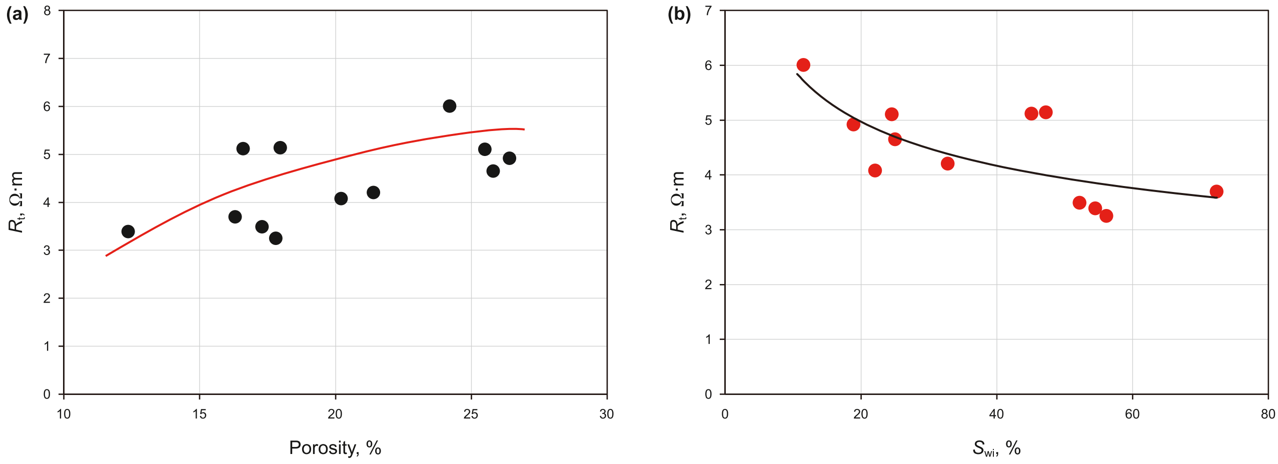

Fig. 11. Crossplot of logging and experimental data from oil-bearing cores. **(a)** R_t–ϕ crossplot, **(b)** R_t–S_{wi} crossplot.

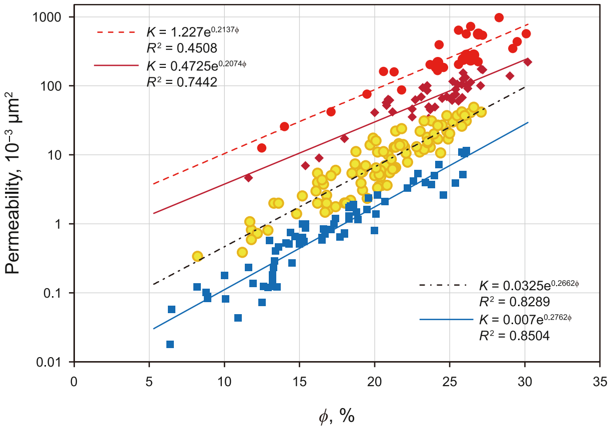

Fig. 12. Crossplot of core porosity and permeability.

(equivalent NaCl salinity: 30386 mg/L), yielding $R_{wf} = R_{wi} = 0.075$ Ω m. According to Eq. (8), since $P_w > P_{w0}$, it follows that $\alpha = 1$. Subsurface temperature (T) was calculated using the formula $T = 18 + 3.41 \cdot H/100$, where H represents depth in meters. Clay-bound water resistivity (R_{wc}) was derived via Eq. (5). Incorporating 2,690 datasets (ϕ_c, ϕ_i, ϕ_f, R_{wf}, R_{wi}, R_{wc}, R_0) into the overdetermined system (Eq. (4)), least-squares optimization resolved the porosity exponents: $m_f = 1.4245$, $m_i = 2.358$, $m_c = 2.29$.

In this paper, shale volume was determined using the spontaneous potential (SP) log. Following correlation analysis between core-derived porosity measurements and three porosity-sensitive logging curves, the density and neutron logs were integrated to compute porosity estimates:

$$\phi = 391.6975 - 157.451 \cdot \mathrm{DEN} + 0.157 \cdot \mathrm{CNL} \tag{17}$$

Owing to high shale content and inherent heterogeneity, permeability depends strongly on pore throat radius and pore structure. Consequently, permeability quantification is conducted after reservoir pore structure classification, with both the categorization scheme and corresponding permeability model presented in Fig. 12.

In this analysis, a notable correlation exists between irreducible water saturation and shale content, porosity, and permeability parameters. The empirical model for quantifying irreducible water saturation was established through rigorous examination of core-derived datasets, with the functional relationships expressed as:

$$\lg(S_{wi}) = 1.3522 + 0.15 \cdot V_{sh} - 0.4119 \cdot \lg\left(\sqrt{K/\phi}\right) \tag{18}$$

To ensure sample consistency, conventional logging data from the same 11 water-saturated intervals selected for porosity exponent calculation were used to determine the clay-bound water volumetric coefficient A. Due to the difference in sampling interval compared with NMR logging, a total of 169 conventional logging data samples were selected. Using Eqs. (10)–(12) and (16)–(18), the pore component volumes (ϕ_c, ϕ_i, ϕ_f) were computed for each measurement point. These parameters, combined with previously derived resistivity values (R_{wf}, R_{wi}, R_{wc}), fully water-saturated resistivity (R_0), and porosity exponents (m_f, m_i, m_c), were incorporated into Eq. (14). The system was solved through least-squares optimization, yielding a clay-bound water volumetric coefficient $A = 0.317$.

Twenty-eight pressurized core samples from adjacent depth intervals were selected. For each core sample, the parameters ϕ_c, ϕ_i, ϕ_f, R_{wf}, R_{wi}, and R_{wc} were calculated using the method described in the preceding step. The corresponding depth-matched resistivity log reading was utilized as R_t. Experimentally measured oil and water saturations underwent volatile correction. The corrected core water saturation (S_w) was then converted to movable water saturation (S_{wf}). These parameters for all 28 cores, along with the previously calculated m_f, m_i, m_c and A, were substituted into Eq. (15) to form an overdetermined system of equations. Least-squares solution of this system yielded $n_f = 1.658$.

3.2.2. Water saturation calculation

Following parameter determination, according to the conventional logging expression Eq. (16) of the triple-water resistivity model, the derived expression for movable water saturation (S_{wf}) is formulated as:

$$S_{\mathrm{wf}} = \sqrt[n_f]{\left[\frac{1}{R_{\mathrm{t}}} - \frac{1}{R_{\mathrm{w}}}\left(\phi \cdot S_{\mathrm{wi}} - V_{\mathrm{q}} \cdot A \cdot \phi \cdot V_{\mathrm{sh}}\right)^{m_{\mathrm{i}}} - \frac{1}{R_{\mathrm{wc}}}\left(V_{\mathrm{q}} \cdot A \cdot \phi \cdot V_{\mathrm{sh}}\right)^{m_{\mathrm{c}}}\right] \Big/ \left[\frac{1}{R_{\mathrm{w}}}\left(\phi - \phi \cdot S_{\mathrm{wi}}\right)^{m_{\mathrm{f}}}\right]} \tag{19}$$

This formulation demonstrates that all required input parameters correspond to conventional well logging measurements, enabling universal application across study area wells. Based on Eqs. (1), (12) and (13), the movable water saturation can be expressed as follows:

$$S_{\mathrm{wf}} = \frac{\phi \cdot S_{\mathrm{w}} - (\phi_{\mathrm{i}} + \phi_{\mathrm{c}})}{\phi_{\mathrm{f}}} = \frac{S_{\mathrm{w}} - S_{\mathrm{wi}}}{1 - S_{\mathrm{wi}}} \tag{20}$$

For well logging interpretation, the total water saturation (S_{w}) is ultimately required. This is calculated using S_{wf} derived from Eq. (19) and the relationship between S_{wf} and S_{w} given by Eq. (20), thereby determining S_{w} according to the following formula:

$$S_{\mathrm{w}} = S_{\mathrm{wf}}(1 - S_{\mathrm{wi}}) + S_{\mathrm{wi}} \tag{21}$$

3.3. *Analysis and discussion of results*

Fig. 13 illustrates water saturation calculations for a segment of the formation in the applied example. The first three tracks display conventional well logs (GR, SP, CAL, DEN, AC, array induction resistivity). Track 5 shows the lithology profile from mud logging, and track 6 presents clay content and porosity. Track 7 reveals that the five tested production layers exhibit co-occurrence of oil and water. Track 8 presents results from the NMR logging interpretation, where green fill denotes clay-bound water volume, gray diagonal hatching represents capillary-bound water volume, and blue fill indicates movable water volume. Track 9 displays volumes of clay-bound water (POR_Wc), capillary-bound water (POR_Wi), and movable water (POR_Wf) computed using the triple-water resistivity model, using identical fill patterns to those in Track 8 for consistency. Track 10 shows saturation values derived from the triple-water model calculations: the red curve represents total water saturation, while the black curve indicates bound water saturation (corresponding to the combined volume of capillary-bound water and clay-bound water). Blue fill signifies movable water saturation within the total pore system, and red fill indicates hydrocarbon saturation within the total pore space. Track 11 presents NMR-derived total water saturation, Track 12 displays water saturation calculated via the shaly sand parallel conductivity equation (SPCE) (Eq. (22)), and Track 13 shows Archie's formula-derived water saturation. In the shaly sand parallel conductivity equation, parameter definitions align with those of triple-water model framework. The petrophysical parameters used in Archie's equation and the shaly sand parallel conductivity model are derived from petrophysical experiments. These experiments yield an integrated petrophysical parameter that can be utilized in both

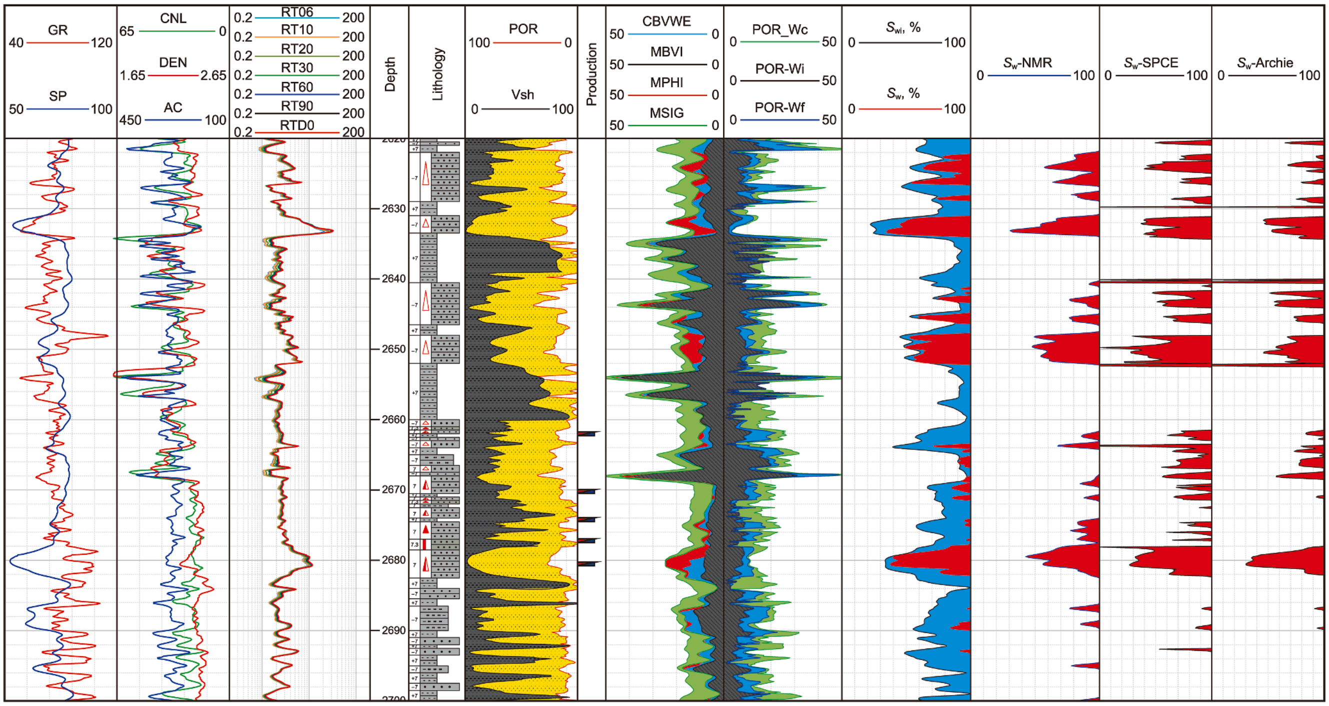

Fig. 13. Results of water saturation calculations for the triple-water model.

Archie's equation and the shaly sand parallel conductivity model, but that cannot be directly applied within the triple-water conductivity model. The shale resistivity (R_{sh}) is determined from resistivity logs of pure shale formations in adjacent well sections.

$$S_{\text{w}}^{n} = \frac{abR_{\text{w}}}{(1 - V_{\text{sh}})\phi^{m}} \left(\frac{1}{R_{\text{t}}} - \frac{V_{\text{sh}}}{R_{\text{sh}}} \right) \tag{22}$$

NMR logging, which is recognized as a sophisticated petrophysical evaluation technique, provides high-resolution formation evaluation data that closely approximate actual subsurface conditions. As illustrated in Fig. 13, the water saturation calculations derived from the triple-water resistivity model demonstrate excellent correlation with NMR-interpreted water saturation values. This alignment is particularly evident in low-resistivity formations and in transitions between sandstone and shale lithologies, where significant discrepancies are observed in saturation estimates obtained from both the Archie's equation and the shaly sand parallel conductivity equation. Notably, these conventional methods exhibit pronounced errors in heterogeneous lithofacies, occasionally yielding non-physical results. Such observations collectively demonstrate the superior performance of the proposed triple-water resistivity model in low-resistivity reservoir characterization, particularly in complex lithological settings where conventional petrophysical models demonstrate limited applicability.

To validate the methodology, a series of comparative analyses were conducted: (1) The parameter estimation employed in this method constitutes a nonlinear least-squares problem. When applied to identical data samples, different optimization algorithms yielded closely matched results; (2) When reservoir intervals were kept consistent for data selection, dataset size was found to have a measurable influence on computational outcomes; (3) Significant variability was observed under conditions of reduced data stability, including large depth separations between samples, heterogeneous reservoir properties across wells, or inherent measurement errors. These findings underscore the critical role of data quality in ensuring calculation accuracy. Consequently, while ensuring the correctness and reliability of the algorithm is essential, greater emphasis must be placed on guaranteeing the accuracy of both the selected data samples and the parameters used within the formula. As shown in Fig. 12, the porosity-permeability crossplot exhibits a generally favorable correlation trend. However, significant data dispersion is observed. To address this, the study classifies the core samples into four distinct categories based on flow units and/or pore structure. Permeability is then calculated separately for each category, leading to a demonstrated improvement in permeability estimation accuracy. This approach also ensures the validity of the multiple parameters utilized in the calculations.

4. Conclusions and recommendations

To address the challenge of hydrocarbon saturation estimation in low-resistivity reservoirs, a triple-water resistivity model parameterization method was developed by integrating NMR-constrained conventional well logging data. The methodology leverages the advantages of NMR logging, which can accurately determine macroporosity, capillary-bound porosity, and clay-bound water porosity. Model parameters are determined through the nonlinear optimization of NMR-constrained well logging datasets. This technique effectively reduces the dependency on extensive core data, thereby significantly improving computational accuracy and reliability. This approach offers dual advantages: 1) reduced dependency on core experimental data through physics-based parameter calibration, and 2) enhanced computational robustness in heterogeneous reservoirs where conventional Archie-based methods exhibit limited performance.

Although positioned as a core-independent solution, the methodology remains consistent with laboratory measurements. Core analysis data, when available, offer valuable constraints for critical parameters (e.g., irreducible water saturation, cementation exponents) and should take precedence in parameterization workflows owing to their direct petrophysical representativeness. The modular implementation allows segmented processing of intervals with interdependent parameters, enabling independent optimization of each calculation module while maintaining mass balance constraints.

This research presents a novel technical framework for hydrocarbon saturation estimation in complex low-resistivity reservoirs. Future optimizations could incorporate: (1) integration of multiple logging modalities beyond NMR and conventional log integration, particularly dielectric dispersion measurements and advanced pulse neutron logs, to improve fluid characterization; and (2) hybrid machine learning architectures combining physics-based models with data-driven algorithms, by leveraging emerging artificial intelligence methodologies for improved handling of nonlinear relationships in heterogeneous reservoir systems. Such advancements would further enhance the applicability of this approach in complex lithofacies settings where conventional petrophysical models demonstrate reduced predictive capability.

CRediT authorship contribution statement

Xue-Juan Zhu: Writing – original draft, Methodology, Formal analysis, Data curation. **Shao-Gui Deng:** Funding acquisition, Conceptualization. **Yi-Ren Fan:** Supervision, Conceptualization. **Xin-Min Ge:** Writing – review & editing, Methodology. **Zhou-Tuo Wei:** Writing – review & editing.

Acknowledgements

This work was supported by the National Natural Science Foundation of China (Grant No. 42374152) and the Natural Science Foundation of Shandong Province (Grant No. ZR2020MD050).

References

Archie, G.R., 1942. The electrical resistivity log as an aid in determining some reservoir characteristics. Petroleum Transactions 146 (1), 54–62. https://doi.org/10.2118/942054-G.

Aguilera, M.S., Aguilera, R., 2003. Improved models for petrophysical analysis of dual porosity reservoirs. Petrophysics 44 (1), 21–35. https://doi.org/10.30632/PJV44N1-2003a1.

Aguilera, R.F., 2004. A triple porosity model for petrophysical analysis of naturally fractured reservoirs. Petrophysics 45 (2), 157–166. https://doi.org/10.30632/PJV45N2-2004a1.

Aguilera, C.G., Aguilera, R., 2009. Effect of fracture dip on petrophysical evaluation of naturally fractured reservoirs. J. Can. Pet. Technol. 48 (7), 25–29. https://doi.org/10.2118/09-07-25.

Al-Ghamdi, Ali, Chen, B., Behmanesh, H., et al., 2011. An improved triple-porosity model for evaluation of naturally fractured reservoirs. SPE Reservoir Eval. Eng. 14 (4), 377–384. https://doi.org/10.2118/132879-PA.

Bukola, K. Olusola, Roberto, Aguilera, 2013. How to estimate water saturation exponent in dual and triple porosity reservoirs with mixed wettability. In: SPE Unconventional Resources Conference–Canada. SPE-167213-MS. https://doi.org/10.2118/167213-MS.

Clavier, C., Coates, G., Dumanoir, J., 1984. Theoretical and experimental bases for the dual-water model for interpretation of shaly sands. SPE J. 24 (2), 153–168. https://doi.org/10.2118/6859-PA.

Dash, S., Heidari, Z., 2022. Development of a universal physics-based resistivity model for estimation of fluid content in unconventional and conventional reservoirs. In: Unconventional Resources Technology Conference. Society of Petroleum Engineers, pp. 2460–2476. https://doi.org/10.15530/urtec-2022-3723594.

Ding, Y.H., 2005. Study on shaly sand three-pore conductivity model log interpretation method.. M. Thesis, Jilin University, pp. 4–81 (in Chinese).

Guo, Y.H., Pan, B.Z., Jiang, B.C., et al., 2015. Tight sandstone reservoir evaluation by the combination of three-water model and mathematical method in Sugeli Area. Geophys. Prospect. Pet. 54 (5), 621–626. https://doi.org/10.3969/j.issn.1000-1441.2015.05.015 (in Chinese).

Huang, B.Z., 2005. A mixture electrical conduction model for shaly sands and its application. Ph.D. Thesis, Jilin University, pp. 27–68 (in Chinese).

Hu, X.Y., Cheng, R.J., Zhang, H.R., et al., 2024. Three-water differential parallel conductivity saturation model of low-permeability tight oil and gas reservoirs. Energies 17 (7), 1726. https://doi.org/10.3390/en17071726.

Iheanacho, P.C., 2013. Formation resistivity theory: How Archie equations, shaly reservoir models, conductive rock matrix model and dual/triple porosity models are related. In: SPE Unconventional Resources Conference–Canada. SPE-167507-MS. https://doi.org/10.2118/167507-MS.

Jia, P., Guo, H.X., Gao, H.D., 2024. Studying the impact of pore sizes on gas flow and distribution involatile carbonate reservoirs using a new triple-porosity model. Phys. Fluids 36 (10), 103. https://doi.org/10.1063/5.0226865.

Kang, N., Hong, X., Zhang, L.H., et al., 2023. Parameters of new three-water model based on nuclear magnetic experiment and optimization algorithm. Glob. Geol. 26 (1), 57–62. https://doi.org/10.3969/j.issn.1673-9736.2023.01.07.

Li, Z.B., Mo, X.W., Wang, Q., et al., 2000. Establishment and application of conductive models for low-resistivity shaly sandstone hydrocarbon reservoirs in the Tarim Basin. Chinese Geological Society. Collection of Important Papers on National Geological Science and Technology Achievements during the Ninth Five-Year Plan, pp. 774–776 (in Chinese).

Mo, X.W., He, D.H., Li, Z.B., et al., 2001. The application of three-water conduction model in the interpretation of low-resistivity reservoir. J. ChangChun Univer. Sci. Tech. 31 (1), 92–95. https://doi.org/10.13278/j.cnki.jjuese.2001.01.019 (in Chinese).

Mo, X.W., Wang, H.J., Xu, S.M., et al., 2005. Log interpretation theory and method to evaluate three pore components in hydrocarbon reservoir formation. J. Jilin Univ. (Earth Sci. Ed.) (S1), 80–83. https://doi.org/10.13278/j.cnki.jjuese.2005.s1.016 (in Chinese).

Poupon, A., Leveaux, J., 1971. Evaluation of water saturations in shaly formations. In: SPWLA 12th Annual Logging Symposium,. SPWLA-1971-O.

Simanjuntak, A.J.S., Jin, J.Y.C., Jo, G., et al., 2020. Managing fluid saturation uncertainties in low resistivity gas reservoirs: A case study from the "X" field in the Baram Delta, Offshore Sarawak, Malaysia. In: SPWLA Asia-Pacific Regional Conference, SPWLA-APRC20-08.

Tariq, Z., Mahmoud, M., Al-Yousef, H., et al., 2018. Non-Archie rock characterization using triple porosity conductivity model in carbonate reservoirs. In: SPE Kingdom of Saudi Arabia Annual Technical Symposium and Exhibition. SPE-192423-MS. https://doi.org/10.2118/192423-MS.

Waxman, M.H., Smits, L.J.M., 1968. Electrical conductivities in oil-bearing shaly sands. SPE J. 8 (2), 107–122. https://doi.org/10.2118/1863-A.

Wei, B., Quan, F.K., Song, Y.X., et al., 2023. Analysis of a middle-rank coal reservoir on a triple porosity/dual permeability model. Nat. Resour. Res. 32, 2197–2222. https://doi.org/10.1007/s11053-023-10232-1.

Xu, X.F., 2012. Logging interpretation and application based on three-water model in fractured tight sand reservoirs. CT Theory App. 21 (2), 221–229 (in Chinese).

Zhang, L.H., Pan, B.Z., Li, Z.B., et al., 2010. New three-water conduction model and its application in evaluation of low porosity and low permeability reservoir. Petrol. Geophy. Prosp. 45 (3), 431–435. https://doi.org/10.13810/j.cnki.issn.1000-7210.2010.03.025 (in Chinese).

Zhang, L.H., Pan, B.Z., Li, N., et al., 2011. Reservoir classification method based on three water model to evaluate low porosity and low permeability reservoir. Well Logging Technol. 35 (1), 31–35. https://doi.org/10.16489/j.issn.1004-1338.2011.01.007 (in Chinese).

Zhang, F., Liu, X.G., Hu, X.X., 2012. Effects of pore structure to conventional well log evaluation in low permeability sandstones. In: SPETT 2012 Energy Conference and Exhibition. SPE-156513-MS. https://doi.org/10.2118/156513-MS.

Zhang, F.J., Deng, S.G., Zhao, H., et al., 2022. A new hybrid method based on sparrow search algorithm optimized extreme learning machine for brittleness evaluation. J. Appl. Geophys. 207, 104845. https://doi.org/10.1016/j.jappgeo.2022.104845.

Zhang, L.H., Pan, B.Z., Shan, G.Y., et al., 2023. A new three-water model based on the complex resistivity-NMR joint survey experiment. Geophys. Geochem. Explor. 47 (4), 1018–1023. https://doi.org/10.11720/wtyht.2023.1481 (in Chinese).